

Maximum Power Point Tracking Techniques for Efficient Photovoltaic Microsatellite Power Supply System

Hadi Malek Sara Dadras, YangQuan Chen
ECE Dept. of Utah State University, Logan, Utah;
Hadi.Malek@energydynamicslab.com
YangQuan.Chen@usu.edu

Robert Burt, James Cook
Space Dynamics Laboratory
1695 N. Research Parkway, North Logan, Utah; 435-713-3337
Robert.Burt@sdl.usu.edu

ABSTRACT

Due to limited power availability and constraints imposed on satellite mass, volume, and available area for photovoltaic (PV) panels, high power conversion efficiency is an important goal in the design process of an electrical power source for microsatellites. In this research, we model, design, and build a photovoltaic based Electrical Power System (EPS) for a satellite to ensure the supply of maximum power and stable operation.

This paper presents the results of our MPPT (maximum power point tracking) research. We describe the EPS power system boundary requirements used in our research. We also describe the design constraints used in our research that are typical to the microsatellite class missions such as extremely low power requirements, limited volume, and minimal, fixed point, processing capabilities. We describe our implementation approach based on proposed algorithms such as Integer Order Extremum Seeking Control (IO-ESC), and Fractional Order Extremum Seeking Control (FO-ESC). Comparison results for the different algorithms are presented as implemented in both the model and on the actual hardware. These new MPPT techniques offer higher conversion efficiency relative to the Perturb & Observe (PO) and other techniques conventionally used in satellite power supply systems.

INTRODUCTION AND HISTORY

There has been a recent increase in emphasis on nanosatellites because of their low cost, short development times, relative simplicity, and cost efficiency. However, these small satellites do have drawbacks. The small size of nanosatellites results in very little surface area which often translates into thermal and power constraints. These small satellites often do not have enough surface area for traditional solar panels. For nanosatellites, it is desirable to use high efficiency solar power systems to maximize the power output from the very limited available area. The system includes the solar cell, the battery, and the power management and distribution (PMAD).

Both SDL and the Center for Self-Organizing and Intelligent Systems (CSOIS) from the ECE department of Utah State University began to independently develop MPPT algorithms and applications. USU's primary focus has been at the algorithm level with a strong focus on theory and simulation. SDL's primary focus has been on nanosat implementation, using the basic P&O algorithm. The goal was to build an EPS for

the PEARL spacecraft. In 2011, SDL and USU combined efforts to marry the algorithm research with the hardware development at SDL.

In 2010, SDL began researching MPPT algorithms for use in FPGA based designs. SDL looked at Perturb and Observe, Incremental conductance, and voltage monitoring methods. The P&O algorithm was initially selected due to its simplicity.

Once SDL and USU teamed, USU suggested using an Extremum Seeking Control algorithm as a potential candidate for flight applications. Two specific versions of the ESC were considered and the integer order version was selected for the first instantiation on the EPS controller. The process of coding the algorithm and implementing them in firmware is somewhat time consuming, so the approach was to implement both the P&O algorithm and the Integer Order ESC (IO-ESC) algorithm into the firmware. In addition to the EPS control hardware, USU possesses a horse power dynamometer used to test control algorithms in a real world environment. The dynamometer is computer

controlled such that algorithms can quickly be implemented and tested via software. The dynamometer was used to compare the IO-ESC algorithm and Fractional Order ESC (FO-ESC) algorithm. The PEARL EPS controller was used to compare the P&O and the IO-ESC algorithms. Prior to the actual hardware testing and comparisons, each algorithm was simulated using MatLab to provide a baseline design and enable extrapolations for final result, not readily achievable in hardware implementations.

The research presented in this paper discusses multiple algorithms. The rest of this paper is organized as follows: In Section II, the photovoltaic characteristics of the solar array are presented. Section III-V, introduces, and discusses the different algorithms used in the research. Section VI presents simulation result for the two extremum seeking algorithms. Sections VII – IX are the experimental results and conclusions.

PV CHARACTERISTICS

Since PV panels exhibit a non-linear Power-Voltage characteristic, their power output mainly depends on the nature of the connected load. Beside this nonlinearity, the maximum power of the PV panel varies by varying environmental condition like irradiation and temperature (Figure 1). Maximizing the power, which is essential, can be achieved by replacing the direct connected PV systems by PV systems having an intermediate maximum power point tracker (Figure 2).

Many maximum power point tracking techniques for photovoltaic systems have been developed to maximize the energy output and lots of these are well established in the literatures: Open-Circuit Voltage (OV), Short-Circuit Current (SC), Fuzzy Logic Control, Ripple Correlation Control (RCC), Current Sweep (SC), Perturb and Observe (P&O) and etc.^{1,2} These techniques vary in many aspects as: simplicity, convergence speed, digital or analogical implementation, sensors required, cost, and etc.

Currently, the most popular MPPT algorithm is perturb and observe (P&O) method, because of its balance between performance and simplicity. Although this algorithm benefits from simplicity, it lacks the speed and adaptability necessary for tracking fast transients in weather. A promising new robust MPPT algorithm is Extremum Seeking Control (ESC), which is closely related to the ripple correlation control (RRC) and P&O methods. It takes advantage of the P&O method simplicity and the robustness and convergence speed of RRC method.

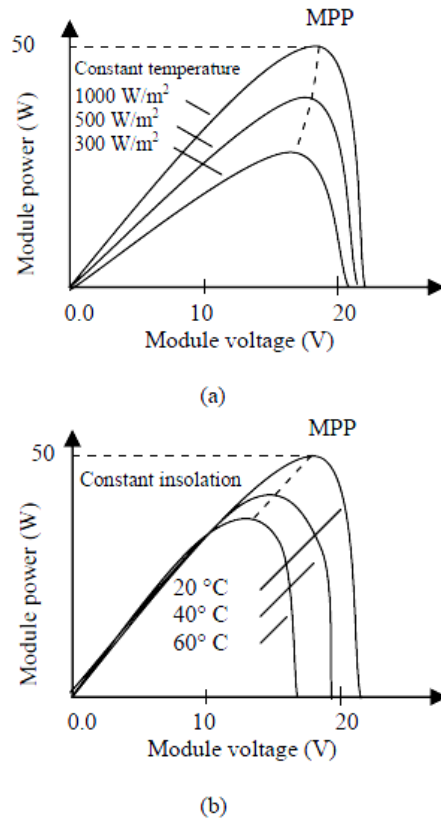


Figure 1- Nonlinear behavior of solar arrays

The ESC method of Krstic³ offers fast convergence and good steady-state performance with guaranteed stability for a range of parameters.

For the first time, in this paper, we will present the fixed point implementation of the integer order ESC algorithm. We will also introduce fractional order ESC control.

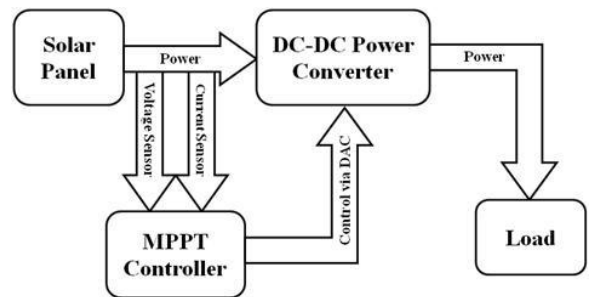


Figure 2-General Scheme of Solar Array with MPPT

PERTURB & OBSERVE WITH BATTERY MANAGEMENT

The perturb and observe algorithm, Figure 3, uses a traditional approach of dithering around the peak power point. The solar array input voltage and current is sampled. The current power value is compared to the previous power value. A control step value is then commanded based on the power comparison results and which side of the power maximum we are on. The peak power is maintained by repeating this process at the correct frequency to match the hardware dynamics. In addition to the peak power tracking capability, this implementation adds multiple step sizes to increase the response speed when conditions our out of bounds of typical solar array bounds. The algorithm is also implemented with a battery management controller since the ultimate end item use is for spacecraft electrical power systems.

This algorithm benefits from knowing specifics about the solar array being attached, such as the array size, and configuration. Using this information helps limit the number permeations possible with every data sample and limits the cases where the algorithm can be confused. This feature limits the universal application of the specific implementation but since only a few number of values are custom for each implementation they are easily made programmable and can be uploaded and modified as necessary.

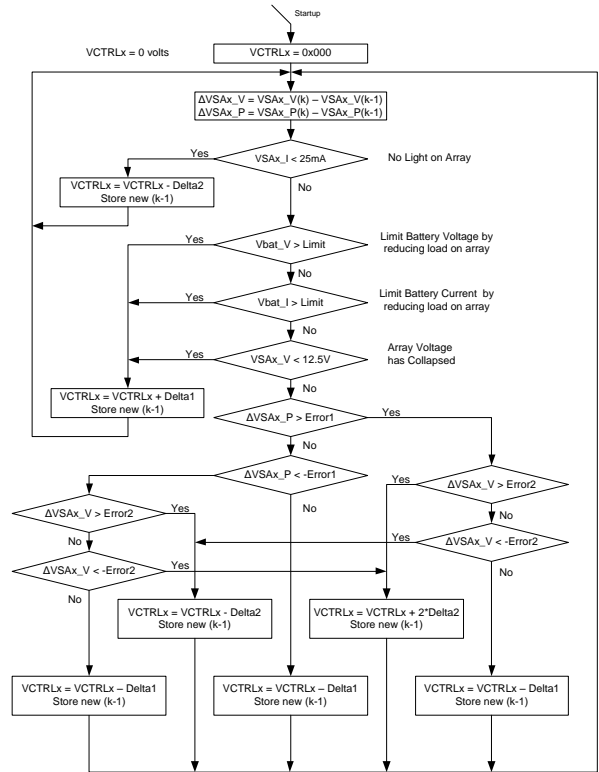


Figure 3-Perturb & Observe Algorithm Flow Diagram

INTEGER ORDER EXTREMUM SEEKING CONTROL

To maximize the PV array power output, we employ an Integer Order Extremum Seeking (IOES) scheme^{3,5} for static nonlinear maps, shown in Figure 4.

The control scheme applies a periodic perturbation $a_0 \sin(\omega t)$ to the duty ratio signal \hat{d} , which is the current estimate of the optimum duty ratio d^* . Assuming the boost DC/DC converter dynamics can be approximated as instantaneous⁶, the sinusoidal varying duty ratio imposes a sinusoidal varying input voltage. This voltage passes through the static nonlinearity $f(\hat{d} + a_0 \sin(\omega t))$, representing the PV array's $P-V$ characteristic curve, to produce a periodic power output p .

The high-pass filter $s / (s + \omega_h)$ then eliminates the DC component of p , and will be in phase or out of phase with the perturbation signal $a_0 \sin(\omega t)$ if \hat{d} is less than or greater than d^* , respectively. This property is important, because when the signal η is multiplied by

the perturbation signal $\sin(\omega t)$, the resulting signal has a DC component that is greater than or less than zero if \hat{d} is less than or greater than d^* , respectively. This DC component is then extracted by the low-pass filter $\omega_l / (s + \omega_l)$. Therefore, the signal ξ can be thought of as the sensitivity $(a_0^2 / 2) \frac{\partial f}{\partial d}(\hat{d})$ and we may use the gradient update $\dot{\hat{d}} = k(a_0^2 / 2) \frac{\partial f}{\partial d}(\hat{d})$ to force \hat{d} to converge to d^* and control goal is achieved.

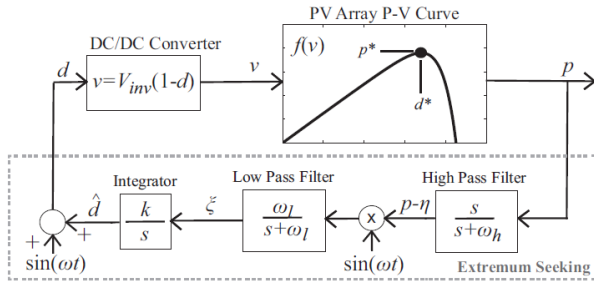


Figure 4-Block diagram of proposed integer order extremum seeking control system [12]

Fixed Point Extremum Seeking Control implementation

Implementing the fixed point ESC algorithm in an FPGA was very challenging due to the architecture limitations of the FPGA and surrounding subsystems. A floating-point core was ruled out at the very beginning of the design phase due to several key reasons. The first reason is the desire for an FPGA design to use minimal power. Floating point cores take up a significant amount of real estate within the FPGA. A larger FPGA is required to implement the floating point core. Larger FPGA's require more static and dynamic power, therefore, the floating-point implementation consumes more power. The second reason is that the input voltages and currents are digitized using an A/D converter. The digitized input voltages and currents are quantized to xxx mV/bit and yyy uA/bit. These numbers don't have infinite resolution. Therefore, having a floating-point core doesn't produce any more precision in the ESC algorithm than compared to binary math.

Another limiting factor is the D/A converter used in providing the control voltage to the BCR's. The control voltage has a fixed step size that controls the amount of current the BCR's supply to the battery. The ESC algorithm closes the loop by dithering the control voltage around a certain voltage to produce an average

control voltage between the fixed steps thus allowing the ESC algorithm to increase the efficiencies.

The ESC algorithm implementation approach was to model the algorithm in a Matlab / Simulink environment using floating point math to validate the algorithm. A second ESC Matlab / Simulink algorithm was created using fixed point math which includes binary adders, subtractors, multipliers and dividers. The dividers are simplified using shift registers as a divide by 2^N . The FPGA ESC algorithm was considered completed once the performance of the fixed point and floating point model outputs matched.

FRACTIONAL ORDER EXTREMUM SEEKING CONTROL

In this section, we first present the Fractional Order Extremum Seeking Control (FO-ESC) scheme and then the stability of this method is investigated.

A. Fractional Order Extremum Seeking Control Scheme

A fractional order extremum seeking approach is presented in Figure 5. In this approach the integer order integrator of IO-ESC is replaced by a fractional order integrator. As we will show later, this replacement can improve the convergence speed of ESC algorithm.

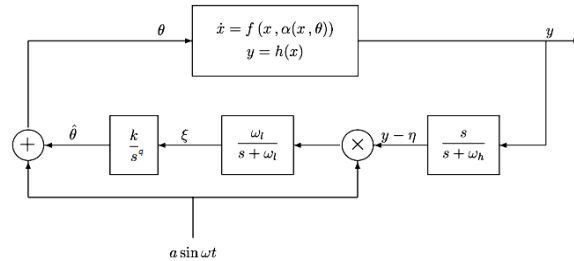


Figure 5-Fractional Order Extremum Seeking Control Scheme

Consider a general single input single output (SISO) nonlinear model

$$\begin{aligned} \dot{x} &= f(x, u) \\ y &= h(x) \\ u &= \alpha(x, \theta) \end{aligned} \quad (9)$$

Assumption 1: There exists a smooth function $l: \mathbb{R}^n \rightarrow \mathbb{R}^m$ such that

$$f(x, \alpha(x, \theta)) = 0$$

$$\text{if and only if } x = l(\theta) \quad (10)$$

Assumption 2: For each $\theta \in \mathbb{R}$, the equilibrium $x = l(\theta)$ of the system $\dot{x} = f(x, \alpha(x, \theta))$ is locally exponentially stable with decay and overshoot constants uniform in θ .

Assumption 3: There exist $\theta^* \in \mathbb{R}$ such that

$$\begin{aligned} (h \circ l)'(\theta^*) &= 0 \\ (h \circ l)''(\theta^*) &< 0 \end{aligned} \quad (11)$$

Based on the Figure 1, we have

$$\begin{aligned} \dot{x} &= f(x, \alpha(x, \hat{\theta} + a \sin(\omega t))), \\ D^q \hat{\theta} &= k \xi, \\ \dot{\xi} &= -\omega_l \xi + \omega_l (y - \eta) a \sin(\omega t), \\ \dot{\eta} &= -\omega_h \eta + \omega_h y. \end{aligned} \quad (12)$$

where D^q is the fractional order Reimann-Liouville integrator⁸.

B. Stability of Fractional Order Extremum Seeking Control

Let us introduce new coordinates

$$\begin{aligned} \tilde{\theta} &= \hat{\theta} - \theta^* \\ \tilde{\eta} &= \eta - h \circ l(\theta^*) \end{aligned} \quad (13)$$

Then, in the time scale $\tau = \omega t$, the aforementioned system is rewritten as

$$\begin{aligned} \omega \frac{dx}{d\tau} &= f(x, \alpha(x, \theta^* + \tilde{\theta} + a \sin(\tau))) \\ \frac{d}{d\tau} \begin{bmatrix} \tilde{\theta} \\ \xi \\ \tilde{\eta} \end{bmatrix} &= \delta \begin{bmatrix} D^{1-q} (K' \xi) \\ -\omega'_L \xi + \omega'_L (h(x) - h \circ l(\theta^*) - \tilde{\eta}) a \sin(\tau) \\ -\omega'_H \tilde{\eta} + \omega'_H (h(x) - h \circ l(\theta^*)) \end{bmatrix} \end{aligned} \quad (14)$$

where

$$\begin{aligned} D^q \hat{\theta} &= k \xi \\ \Rightarrow \dot{\hat{\theta}} &= D^{1-q} (k \xi) \end{aligned} \quad (15)$$

For the stability analysis, we need to freeze “ x ” in its equilibrium value

$$x = l(\theta^* + \tilde{\theta} + a \sin(\tau)) \quad (16)$$

Then, we have

$$\frac{d}{d\tau} \begin{bmatrix} \tilde{\theta}_r \\ \xi_r \\ \tilde{\eta}_r \end{bmatrix} = \delta \begin{bmatrix} D^{1-q} (K' \xi_r) \\ -\omega'_L \xi_r + \omega'_L (v(\tilde{\theta}_r + a \sin(\tau)) - \tilde{\eta}_r) a \sin(\tau) \\ -\omega'_H \tilde{\eta}_r + \omega'_H v(\tilde{\theta}_r + a \sin(\tau)) \end{bmatrix} \quad (17)$$

where

$$\begin{aligned} v(\tilde{\theta}_r + a \sin(\tau)) &= h \circ l(\theta^* + \tilde{\theta}_r + a \sin(\tau)) \\ &\quad - h \circ l(\theta^*) \end{aligned} \quad (18)$$

Using assumption 3, one can easily conclude

$$\begin{aligned} v(0) &= 0, \\ v'(0) &= (h \circ l)'(\theta^*) = 0, \\ v''(0) &= (h \circ l)''(\theta^*) < 0. \end{aligned} \quad (19)$$

Now, using the averaging method⁹, we have

$$\frac{d}{d\tau} \begin{bmatrix} \tilde{\theta}_r^a \\ \xi_r^a \\ \tilde{\eta}_r^a \end{bmatrix} = \delta \begin{bmatrix} D^{1-q} (K' \xi_r^a) \\ -\omega'_L \xi_r^a + \frac{\omega'_L}{2\pi} a \int_0^{2\pi} v(\tilde{\theta}_r^a + a \sin(\sigma)) \sin(\sigma) d\sigma \\ -\omega'_H \tilde{\eta}_r^a + \frac{\omega'_H}{2\pi} a \int_0^{2\pi} v(\tilde{\theta}_r^a + a \sin(\sigma)) d\sigma \end{bmatrix} \quad (20)$$

First, we need to determine the average equilibrium $(\tilde{\theta}_r^{a,e}, \xi_r^{a,e}, \tilde{\eta}_r^{a,e})$ which satisfies

$$\begin{aligned} \xi_r^{a,e} &= cte, \\ \xi_r^{a,e} &= \frac{1}{2\pi} \int_0^{2\pi} v(\tilde{\theta}_r^{a,e} + a \sin \sigma) \sin \sigma d\sigma \\ \tilde{\eta}_r^{a,e} &= \frac{1}{2\pi} \int_0^{2\pi} v(\tilde{\theta}_r^{a,e} + a \sin \sigma) d\sigma \end{aligned} \quad (21)$$

Then

$$\begin{aligned} \xi_r^{a,e} &= cte, \\ \xi_r^{a,e} &= \frac{1}{2\pi} \int_0^{2\pi} v(\tilde{\theta}_r^{a,e} + a \sin \sigma) \sin \sigma d\sigma \\ \tilde{\eta}_r^{a,e} &= \frac{1}{2\pi} \int_0^{2\pi} v(\tilde{\theta}_r^{a,e} + a \sin \sigma) d\sigma \end{aligned} \quad (22)$$

By postulating $\tilde{\theta}_r^{a,e}$ in the form

$$\tilde{\theta}_r^{a,e} = b_1 a + b_2 a^2 + O(a^3), \quad (23)$$

we get

$$\begin{aligned} v''(0)b_1 &= 0, \\ v''(0)b_2 + \frac{1}{8}v'''(0) &= 0 \end{aligned} \quad (24)$$

which implies

$$\tilde{\theta}_r^{a,e} = -\frac{v'''(0)}{8v''(0)}a^2 + O(a^3). \quad (25)$$

These results in

$$\tilde{\eta}_r^{a,e} = \frac{v''(0)}{4}a^2 + O(a^3). \quad (26)$$

Thus, the equilibrium of the average model is

$$\begin{bmatrix} \tilde{\theta}_r^{a,e} \\ \xi_r^{a,e} \\ \tilde{\eta}_r^{a,e} \end{bmatrix} = \delta \begin{bmatrix} -\frac{v'''(0)}{8v''(0)}a^2 + O(a^3) \\ 0 \\ \frac{v''(0)}{4}a^2 + O(a^3) \end{bmatrix}. \quad (27)$$

The Jacobian matrix at $(\tilde{\theta}, \xi, \tilde{\eta})_r^{a,e}$ for the above system is

$$J_r^a = \delta \begin{bmatrix} 0 & \Psi & 0 \\ \frac{\omega'_L}{2\pi} a \int_0^{2\pi} v'(\tilde{\theta}_r^{a,e} + a \sin(\sigma)) \sin(\sigma) d\sigma & -\omega'_L & 0 \\ \frac{\omega'_H}{2\pi} \int_0^{2\pi} v'(\tilde{\theta}_r^{a,e} + a \sin(\sigma)) d\sigma & 0 & -\omega'_H \end{bmatrix} \quad (28)$$

Since J_r^a is block-lower-triangular, it can be concluded that it will be Hurwitz if and only if

$$\int_0^{2\pi} v'(\tilde{\theta}_r^{a,e} + a \sin(\sigma)) \sin(\sigma) d\sigma < 0 \quad (29)$$

So, from the previous parts, one can easily conclude

$$\begin{aligned} \int_0^{2\pi} v'(\tilde{\theta}_r^{a,e} + a \sin(\sigma)) \sin(\sigma) d\sigma \\ = \pi v''(0)a + O(a^2) \end{aligned} \quad (30)$$

Then, we get

$$\begin{aligned} \det(\lambda I - J_r^a) \\ = \left(\lambda^2 + \delta \omega'_L \lambda - \frac{\delta^2 \omega'_L K'}{2} v''(0) a^2 + O(\delta^2 a^3) \right) \\ \times (\lambda + \delta \omega'_H) \end{aligned} \quad (31)$$

which proves that J_r^a is Hurwitz for sufficiently small a . This, in turn, implies the equilibrium of the average system is exponentially stable for a sufficiently small a .

SIMULATION RESULTS OF FRACTIONAL ORDER EXTREMUM SEEKING CONTROL

A. Simulation Results

In this section, the IO-ESC and FO-ESC are simulated and compared using the PV model⁴, a boost DC-DC converter, and Simulink/Matlab. Since this algorithm will be applied to a dynamometer, we will be required to use longer rise times because the dynamometer cannot respond as quickly and is therefore limited by the hardware. The output of the ESC block is used as the input to the converter to tune its duty cycle (Figure 6).

Numerical simulations are done in two cases: without and with environmental noise. The results are illustrated in Figure 7 and Figure 8. These simulations are done under the condition $T=25^\circ\text{C}$, $G=1000 \text{ W/m}^2$ and the extremum seeking control gain is set to $k=250$. The noise applied to the model is a uniform noise $\sim U(-0.1, 0.1)$.

It can be seen that in both cases, the FO-ESC converges to the extremum point faster than the IO-ESC. It should be noticed that the applied extremum seeking scheme performance is satisfactory regardless of whichever admissible noise affects the system.

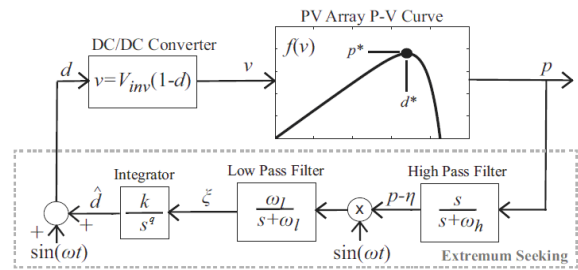


Figure 6-Block diagram of proposed fractional order extremum seeking control system.

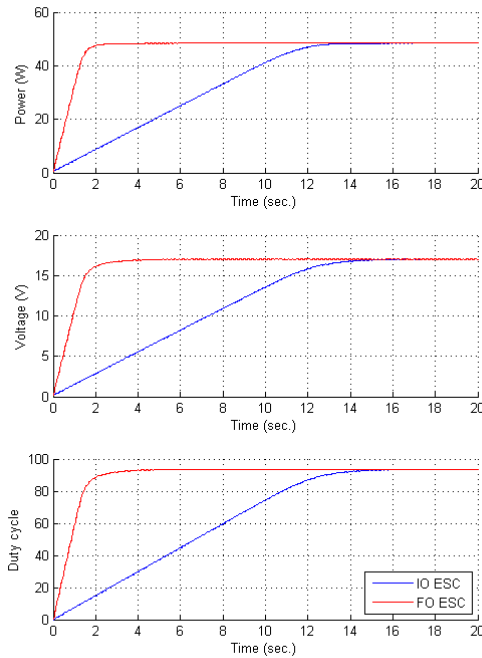


Figure 7-Time response of the PV Module without noise when fractional order ESC is applied ($q=0.95$).

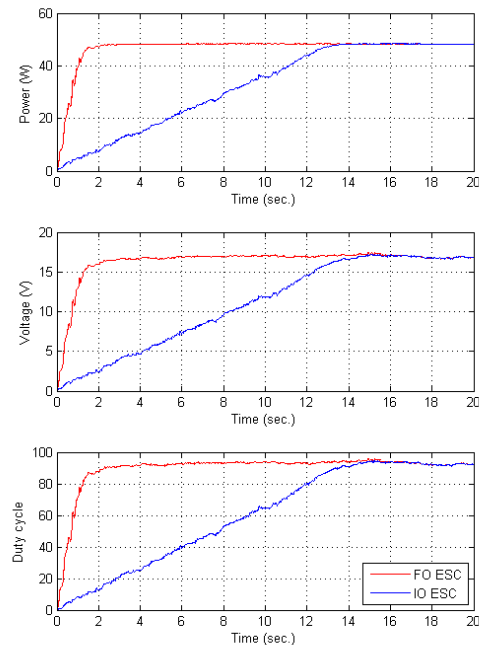


Figure 8-Time response of the PV Module in presence of noise when fractional order ESC is applied ($q=0.95$).

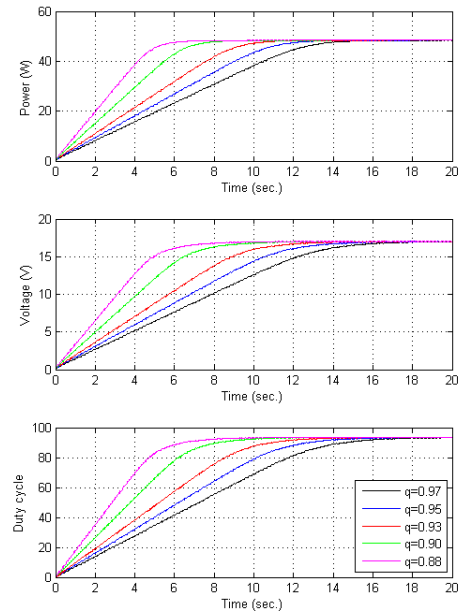


Figure 9-Time responses of the PV module for different integration orders in fractional order ESC.

To show the effect of the fractional integration order, the different simulation are done for a constant arbitrary $k=150$, while q (order of the fractional integrator) is changed in each level. The results are shown in Figure 9. It can be observed that by reducing q , the speed of convergence of the system toward extremum point is increased.

EXPERIMENTAL RESULTS

A. Fractional Horsepower Dynamometer

Since we don't have the resources to implement FO-ESC on the FPGA, we have used another test bench to model the nonlinearity of the PV panels and evaluate the FO-ESC algorithm. This new test bench is the dynamometer.

The dynamometer includes a DC motor, which is coupled with a hysteresis brake, (Figure 11). The nonlinear behavior of the PV panels can be modeled using this hysteresis break. The break output torque can be considered as output current of PV modules. Then the output power is a product of this angular velocity and the current of PV modules. The proposed scheme can be seen in Figure 10.

Without loss of generality, the DC motor in the dynamometer can be approximated by the following transfer function

$$G_m(s) = \frac{1.52}{1.01s + 1} \quad (32)$$

In this benchmark, we are trying to control angular speed of DC motor (which represent the average PWM voltage of DC-DC converter) to extract the maximum torque out of the motor, when a nonlinear system, which represent the PV model, has been applied to the brake.

In this experiment, the extremum seeking control scheme is tested using the Matlab/Simulink environment, which uses the WinCon application, to communicate with the Quanser MultiQ3 data acquisition card. WinCon is a Windows-based application that runs Simulink models in real-time on a PC. This brings rapid prototyping and hardware-in-the-loop simulation capabilities to Simulink models.

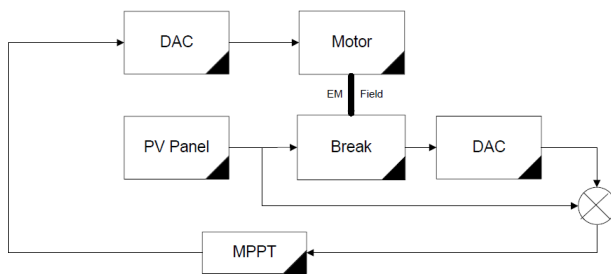


Figure 10-Modeling the PV panel using fractional horsepower dynamometer.

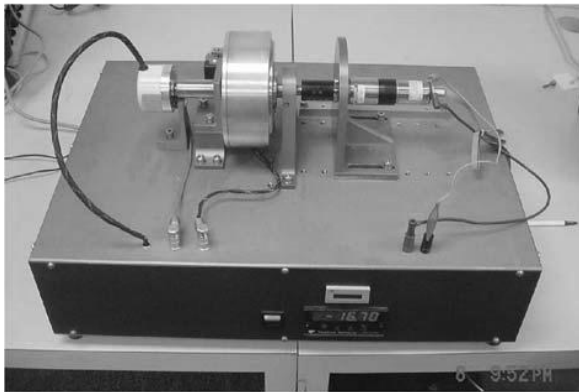


Figure 11-The fractional horse power dynamometer developed at CSOIS¹⁰.

The Simulink model used for the experiments is shown in Figure 12. This figure shows the hardware-in-the-loop real time simulation models for integer order and fractional order extremum seeking scheme,

respectively. It is worth noting that Simulink automatically generates codes for Windows target to drive the dynamometer and brake via D/A blocks.

It can be seen that the proposed ESC scheme can be easily applied to the fractional horsepower dynamometer as the PV model and the results are satisfactory. From the Figure 13 and Figure 14, it can be also noticed that the convergence speed of FO-ESC is better than the IO-ESC which admits the results achieved from numerical simulation results in previous part.

Figure 15 and Figure 16 illustrate that reduction in the order of fractional order integrator can improve the convergence speed of FO-ESC.

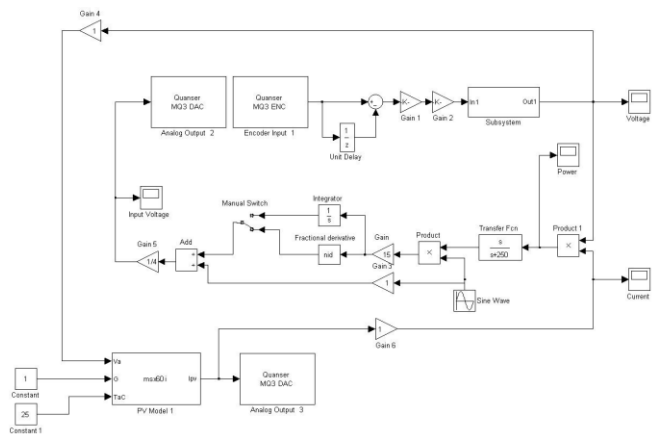


Figure 12-Simulink model used in the fractional order ESC real time experiments using RTW Windows Target

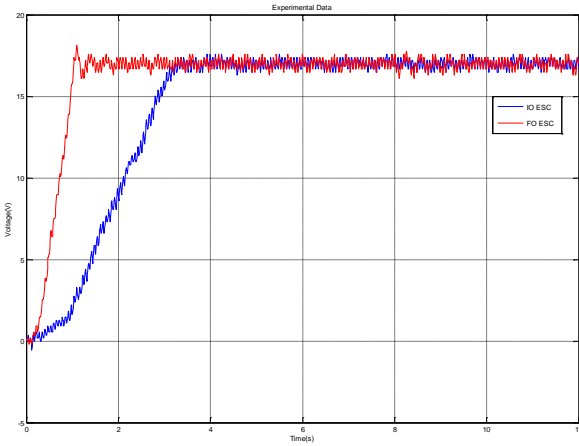


Figure 13-Convergence of PV voltage to extremum point applying IO-ESC and FO-ESC ($q=0.95$).

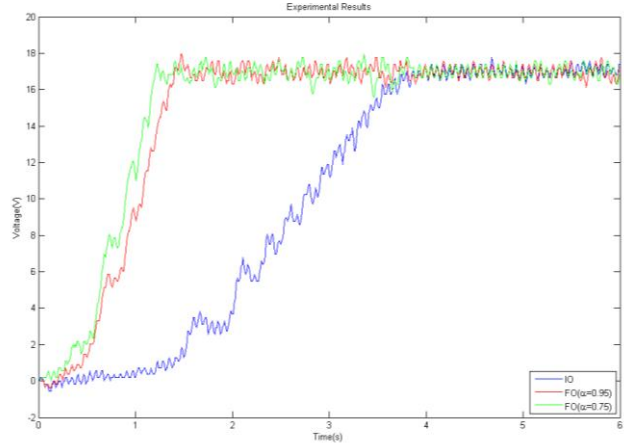


Figure 15-Convergence of PV voltage to extremum point applying different integration orders in IO-ESC and FO-ESC.

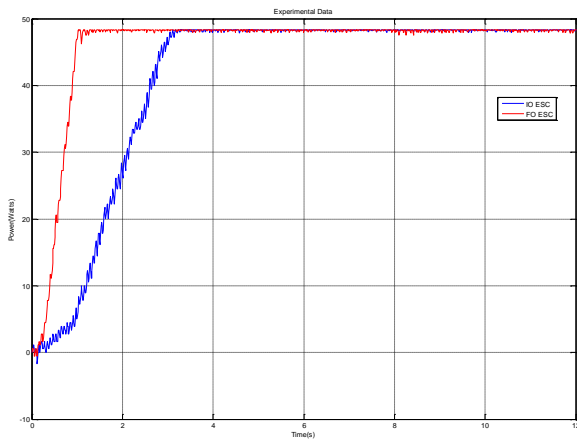


Figure 14-Convergence of PV power to extremum point applying IO-ESC and FO-ESC ($q=0.95$).

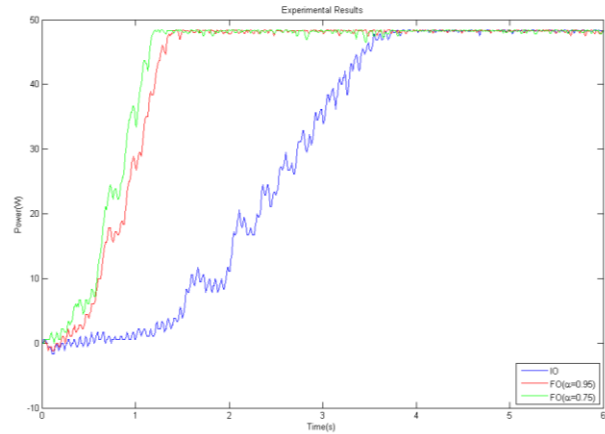


Figure 16-Convergence of PV power to extremum point applying different integration orders in IO-ESC and FO-ESC.

MPPT TEST CONTROLLER HARDWARE REQUIREMENTS AND CONSTRAINTS

Although the cubesat is an ideal platform for an MPPT based EPS, the cubesat design requirements, pose specific challenges to the implementation. SDL has designed an EPS hardware controller that is baselined for the PEARL cubesat. This EPS hardware controller was used as the test bed for algorithm testing. The

following requirements are typical of cubesats and form the basis for this EPS design.

Size and Volume Requirements

This EPS design was specified for a 3U cubesat. A single card is allocated for battery charge management voltage regulation, and power distribution. The battery is not included in this size allocation. The card size is less than 10cm on a side. The component height is less than 11.5 mm on the top and less than 3mm on the bottom. The design requires two separate channels to accommodate two separate solar array inputs. Each input is to implement maximum peak power tracking to maximize the power output of the solar array.

Power Requirements

The goal of the MPPT EPS is to maximize power generation from the solar array and at the same time, minimize the amount of power consumed to accomplish this. The use of ultra-low power components and high efficiency converters is requisite. The design requirement is to handle up to 40 watts input power (20 watts per channel). The EPS is required to be greater than 90% efficient. The quiescent power draw (no load) is required to be less than 200 mW.

EPS Description and Constraints

The EPS, as designed, includes two solar array inputs that feed into separate battery charge regulators (BCR). The BCRs use a buck converter topology implemented with a current mode DC-DC converter. The two converters are tied together at the output where they connect to the battery. The battery is a 3S1P lithium-ion battery rated at 2.25 Amp-hours. There are two switched battery outputs for power distribution along with two regulated power buses of 3.3 volts and 5 volts, see Figure 17 and Figure 18. The MPPT architecture effectively decouples the solar array from the battery and allows for much more flexibility in EPS design than compared to the Direct Energy Transfer (DET).

Voltage and current monitors are placed on each solar array input, the battery, and each of the outputs. An ultra-low power FPGA is used to implement the algorithm and controller. The low power FPGA is a key component. It allows for minimum power dissipation by the EPS and selected due to a higher tolerance to radiation effects over other commercially available components. The low power simple architecture forces all algorithms to use fixed point integer based implementations. This becomes one of the major design constraints for this project.

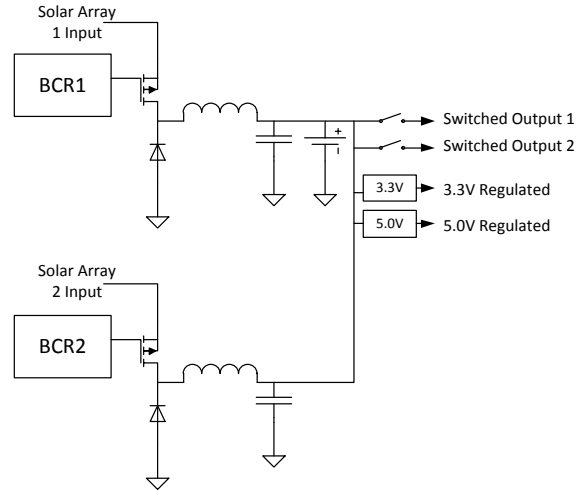


Figure 17 - EPS Electrical Block Diagram

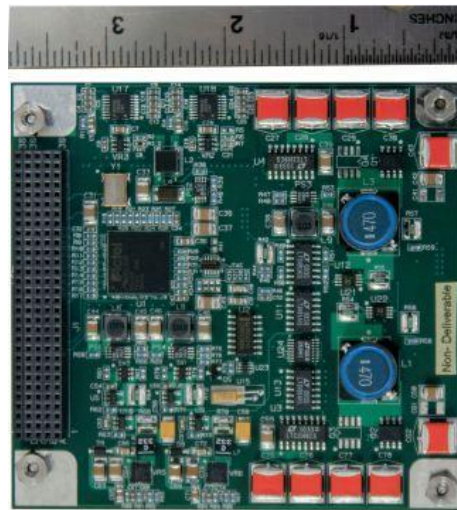


Figure 18 - EPS Controller Card

TEST SET UP

Figure 19 shows the test equipment setup. The solar array simulator is used to generate the IV curve for the hardware algorithm tests. An external power supply is used to provide power to the EPS when the battery is not connected. For consistency sake, most of the testing is done in this configuration. A blocking diode is in series with the external power supply that inhibits the power supply from sinking current. In this manner, it is not consistent with a real battery, as the battery will both sink and source current. A four channel electronic load is used to apply loads at each of the four outputs. The load can be varied as required for each test. Finally, a command, control, and monitor computer is provided that allows the EPS parameters to be configured and the telemetry data, coming from the EPS, to be monitored.

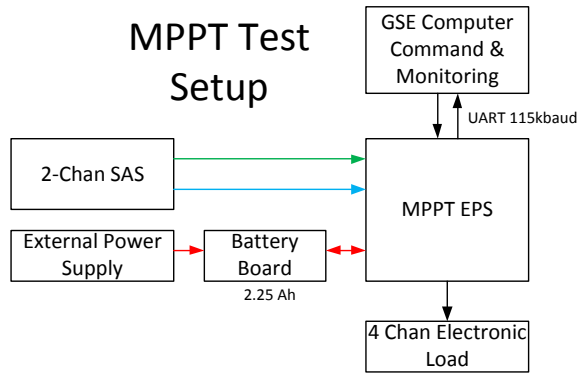


Figure 19 - MPPT EPS Test Setup

Table 1 is the list of test equipment used in the MPPT testing. Other components were used at different stages, including digital multi-meters and oscilloscopes, for specific measurements.

Table 1 - Test Equipment

Manufacture	Model Number	Description
Agilent	E3631	Triple Output Power Supply
Agilent	E4360A	Modular SAS Mainframe
Agilent	E4362	Solar Array Simulator Module
Agilent	E4362	Solar Array Simulator Module
Chroma	6314	Electronic Load Mainframe
Chroma	63102	Dual Channel Load Module
Chroma	63107	Dual Channel Load Module
Dell	M90	Laptop Computer + Monitor

TEST RESULTS AND COMPARISON OF FIXED POINT ESC AND P&O ALGORITHMS

The EPS control hardware is designed to provide telemetry over a serial link. The serial link is run at 115.2kbaud which allows for every sample processed by the algorithm to be output and collected for analysis. The data presented in this section is the full bandwidth unfiltered data. Every sample is collected and displayed.

Five different types of tests were performed on the test hardware using both algorithms. The tests include the following:

Steady State: This test was a 30 second sample in time of the EPS power output with a fixed solar array input. The goal of the test is to determine how well each algorithm tracked the peak power point with no variations on the input.

Ramp Testing: This test provides an input where the Imp and Isc current are varied according to a ramp function. The purpose of this test is to determine how well each algorithm can track a constant rate input variation.

Source Pulse (Step) Testing: This test applies an input where both Imp and Isc currents are stepped in one time increment from a low level to high level and then back down to a low level. The purpose is to see the algorithm's response to the step function input. This test tells us how fast the system will respond to large perturbations

Load Pulse Test: This test maintains a steady state input but varies the output in a step function. The load is stepped from a value less than the peak power to a value greater than the peak power. The goal is to determine how well the controller can respond to abrupt load variations.

Sinusoidal Testing: This last test applied a sinusoidal varying input. Both a full sine wave and a half sine wave were used. The goal of this test was to determine how well the algorithms can respond to a time varying input consistent with actual space flight movements.

Steady State Response Results

The solar array simulator is configured to represent a single string solar array with 7 cells in series. The open circuit voltage, Voc, is 18.65 volts; Vmp is 16.45 volts; Imax power is .433 amps; Isc is .453 amps. A 30 second sample is taken for each channel separately and then for both channels simultaneously. The test is repeated using each algorithm to enable a side by side comparison.

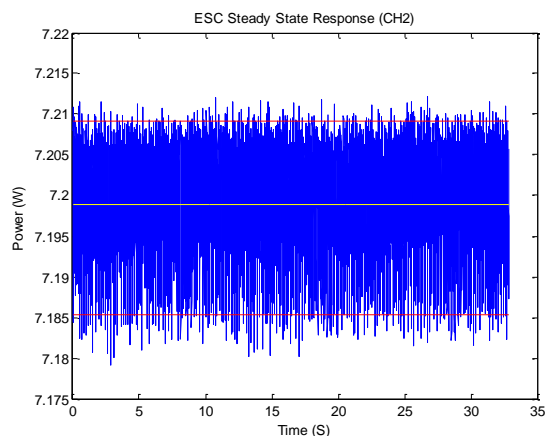


Figure 20-ESC Steady State Response

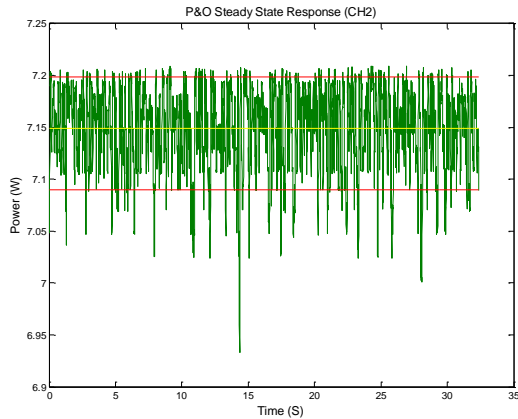


Figure 21- P&O Steady State Response

We looked at four different metrics, see Table 2. The first was Average Power. This is simply the mean value of all of the sampled data. The next are the minimum and the maximum values. These values are the minimum recorded power value and the maximum recorded power value respectively delivered by the solar array. The last value is an average peak to peak value. This parameter averages all of the positive direction peak power values greater than the mean and then subtracts the average of all of the negative direction peaks less than the mean. The difference is the average pk-pk value. It is graphically represented by the red lines in the plot. From the data it is very apparent that the ESC algorithm is out performing the P&O algorithm in the steady state. A summary of the other channels and configuration tested, showed the ESC algorithm to be better in each of the test cases for the steady state. The ESC algorithm was much less sensitive to channel to channel hardware differences. Also the ESC algorithm did not seem to be affected by simultaneous operation of both channels. The performance stayed consistent regardless of which channels were active and when. The P&O algorithm showed more sensitivity between the channel to channel hardware differences. There also appeared some structure in the output plots when both channels were operating together suggesting some sort of channel to channel interaction.

Table 2-ESC Steady State Power Metrics

Metric	ESC Value	P&O Value
Average Peak-to-Peak	0.024 watts	0.109 watts
Average Power	7.199 watts	7.149 watts
Minimum Power Output	7.179 watts	6.933 watts
Maximum Power Output	7.212 watts	7.2093 watts

Dynamic Response Results

The rest of the testing involves either a dynamic source input or a dynamic load. The IO-ESC was implemented without slope seeking control. It therefore is expected to have some decreased performance in the dynamic environments. This is discussed further in our conclusions section.

The following figures, Figure 22 through Figure 25, show the response of the algorithms to four different dynamic inputs. In all cases the load was set to be greater than the maximum available solar array input power. This forces the controller to always try and control to the maximum power point of the input. Both algorithm results are plot together to allow for easy comparison of differences.

For the ramp test, the array is nominally set to $P_{mp} = 1.65$ watts (maximum power point) and then ramped up to $P_{mp} = 8.25$ watts. This is done by varying the solar I_{mp} input current from 0.1 amps to 0.5 amps at a rate of 5ma per 200ms. Both algorithms track the ramp but the ESC exhibits a stutter at the beginning of the ramp

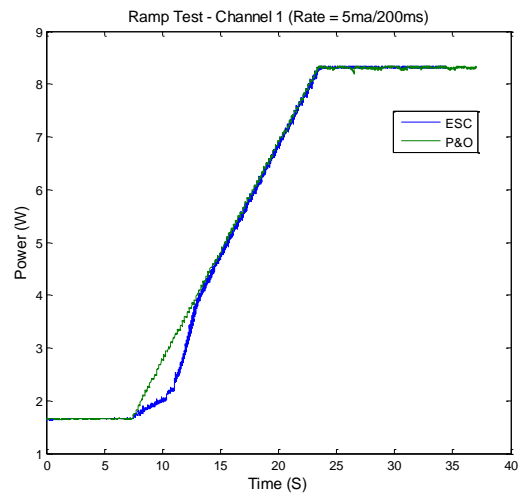


Figure 22- Ramp Test (Rate = 5ma/200ms)

The input source step/pulse test is configured by setting the input to a nominal 1.65 watt peak power point. The source is then step via a single command to 9.87 watts peak. The plot shows the speed of the response to the step input function. Again, the P&O demonstrates a faster response to the rising edge of the step. The falling edge is for all practical purposes the same. Both algorithms require some finite amount of time to re-establish control after the negative step. We should note here that the response shown in the plot is a combination of the entire system and not just the algorithms themselves. The EPS board has a

significant amount of input capacitance that slows the input rise time.

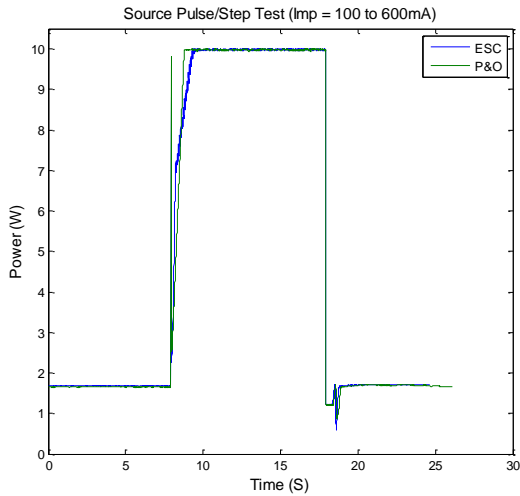


Figure 23-Source Pulse/Step Test. Input steps from 100mA to 600mA.

The next plot shows the results of the full wave sine input. The solar array input is programmed to output a 0.1Hz sine wave with Imp varied between ± 250 ma (± 4.1 watts). The entire input is offset by 350ma to allow a swing between 100mA and 600mA. Again, the load is set to a value greater than the maximum input power level to ensure that the controller is always trying to drive towards the peak power point. The P&O algorithm exhibits very good response to this input and tracks the solar array input very precisely. The ESC algorithm has more trouble. On the rising edge, the algorithm is somewhat delayed but still responsive. On the falling edge, we can see where the algorithm loses control allowing the array to collapse and then it recovers and repeats the scenario until the input starts to rise again. The hardware configuration is an important factor in this collapse. When the input power begins to drop, the net effect is to force the system to the short circuit side of the solar array I-V curve. If the algorithm does not respond fast enough to throttle back the load seen by the array, then the array voltage will collapse down to the battery voltage. Once there, the algorithm cannot simply throttle back to the peak power but rather it must throttle all of the way back to the equivalent voltage current value on the open circuit side of the I-V curve. Once there it can begin to ramp back up to the new peak point. You can see this response in the falling edge of the sinusoidal curve.

The half wave test shows similar results as both the full wave sine test and the input step test. The half wave amplitude is the same as that used in the step test and the speed of rise is sufficiently fast that is close to

looking like the step test. A smaller amplitude or a larger time period would have been more appropriate. Either way, the P&O algorithm tracks the input fairly well with the exception of the small spike on the rising edge similar to that seen on the pulse test. The falling edge looks relatively clean. The ESC algorithm sees the same spike on the rising edge. It also has the same slow response problem on the falling edge as well.

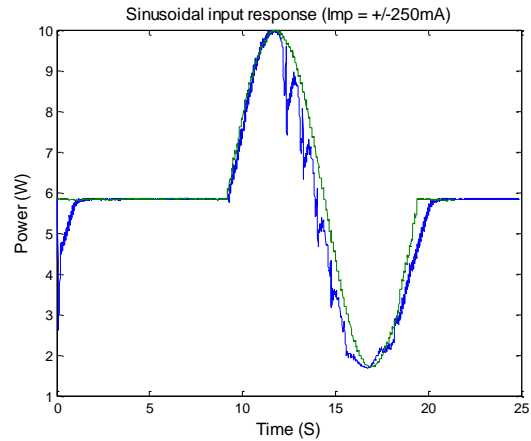


Figure 24- Sinusoidal Input. Imp amplitude = +/-250mA over a 10 second period.

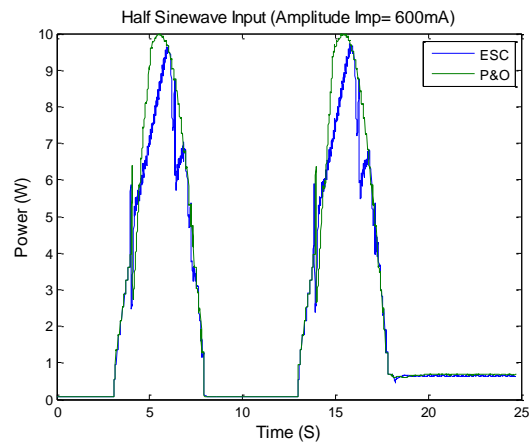


Figure 25- Half wave sine input. Imp Amplitude = 600mA. The period is 10 seconds.

CONCLUSION

In this paper, A Perturb and Observe, IO-ESC, and FO-ESC algorithms are briefly introduced. The proposed extremum seeking control method with both integer order and fractional order integrators are simulated using Matlab/Simulink and the common PV model for two different cases; In presence of environmental noise and without noise. Then, using the fractional horsepower dynamometer, experiments were done to test both extremum seeking algorithms, fractional order

and integer order. In parallel, IO-ESC and the P&O algorithms were experimentally tested using a PV array simulator and the PEARL spacecraft electrical power system as the test bench.

From the experimental results on the dynamometer benchmarks, it can be declared that the fractional order ESC has a better performance in comparison with integer order ESC. Also the experimental results on the PV array simulator and EPS test bench have been discussed in this paper. As we can see in these experiments, in the steady state condition, ESC can extract more power from PV panels, has smaller peak-peak power ripple, and provides greater immunity for channel to channel interference in comparison with P&O controller. In the dynamic response tests, the P&O algorithm clearly outperforms the IO-ESC algorithm as presently implemented.

Because of time constraints, we were not able to implement the slope seeking control portion of the ESC algorithm and compare it to the P&O. Obviously; ESC cannot follow fast slopes and cannot satisfy high dynamic response MPPT requirements as we can see in the experimental results. The ESC algorithm tends to find the extremum point and at this point the slope constantly is equal to zero. When we have a slope which is not zero, like in the ramp condition, we need to add the amount of this slope to the integrator of the ESC algorithm to force the system to follow this non-zero slope instead of following the zero slope. Implementing slope seeking control and improving the maximum power point tracking in the ramp condition will be the focus of follow on work associated with this project.

ACKNOWLEDGMENTS

We would like to acknowledge and thank the Air Force Research Laboratory for providing the funding for this research effort without which it could not have been possible. We would also like to thank the Space Dynamics Laboratory and Utah State University for support of time and other laboratory resources involved in the testing.

References

1. S.L. Brunton, C.W. Rowley, S. R. Kulkarni, C. Clarkson, "Maximum power point tracking for photovoltaic optimization using Ripple-Based extremum seeking," IEEE Transactions On Power Electronics, Vol. 25, pp. 2531-2540, 2010.
2. T. Eswam and P. L. Chapman, "Comparison of photovoltaic array maximum power point tracking techniques," IEEE Transactions On Energy Conversion, vol. 22, pp. 439-449, 2007.

3. K. Ariyur and M. Krstic, Real Time Optimization by Extremum Seeking Control, Wiley, 2003.
4. J. A. Gow, C. D. Manning "Development of a photovoltaic array model for use in powerelectronics simulation studies," IEEE Proceedings on Electric Power Applications, vol. 146, no. 2, pp. 193-200, March 1999.
5. M. Krstic and H.H. Wang, "Stability of extremum seeking feedback for general nonlinear dynamic systems," Automatica, vol. 36, no. 4, pp. 595-601, 2000.
6. B. Johansson, "Improved Models for DC-DC Converters," Department of Industrial Electrical Engineering and Automation, Lund University, 2003.
7. S. Moura, "A switched extremum seeking approach to maximum power point tracking in photovoltaic systems," EECS 498-003 Project, April 2009.
8. I. Polubny, Fractional differential equations. New York: Academic Press, 1999.
9. H. K. Khalil, Nonlinear systems. Prentice Hall Upper Saddle River, NJ, 2002.
10. Y. Tarte, Y.Q. Chen, W. Ren, and K. Moore, "Fractional horsepower dynamometer-A general purpose hardware-in-the-loop real-time simulation platform for nonlinear control research and education," Proc. 45th IEEE Conference on Decision and Control, San Diego, 2006, pp. 3912-3917.